

Defect distribution in ion-irradiated pure tungsten at different temperatures

Zhexian Zhang ^{a, b,*}, Kiyohiro Yabuuchi ^b, Akihiko Kimura ^b

^a Graduate School of Energy Science, Kyoto University, Yoshida-honmachi, Sakyo-ku, Kyoto 606-8501, Japan

^b Institute of Advanced Energy, Kyoto University, Gokasho, Uji, Kyoto 611-0011, Japan



ARTICLE INFO

Article history:

Received 2 March 2016

Received in revised form

23 August 2016

Accepted 24 August 2016

Available online 25 August 2016

Keywords:

Tungsten

Ion irradiation

TEM

Microstructure distribution

Grain boundary effect

ABSTRACT

Tungsten (W) has been selected as the armor materials for divertor in fusion reactors. To investigate the temperature dependent microstructural evolution under fusion relevant environment, pure W was irradiated with dual beam of 6.4 MeV Fe³⁺ and 1 MeV energy degraded He⁺ at 300 °C, 500 °C, 700 °C and 1000 °C. The overall distribution of microstructures were observed. At 300 °C, a high dislocation density zone (HDDZ) appeared at the end of radiation area. The HDDZ gradually disappeared with increasing irradiation temperature, instead, a low dislocation density zone (LDDZ) appeared between the front zone (FZ) and diffusion zone (DZ). At all the irradiation temperatures, both dislocation lines and loops were observed, while bubbles were observed only at 500 °C and above. Loop rafts appeared in the whole irradiated area from 300 °C to 700 °C, but only in the defect diffusion zone (DZ) at 1000 °C. Dislocation loop denuded zone was formed along grain boundaries, suggesting that grain boundaries suppress the formation of dislocation loops. Bubbles at grain boundaries tended to have a larger size than those in the matrix, indicating that bubble growth was accelerated in grain boundaries.

© 2016 Elsevier B.V. All rights reserved.

1. Introduction

Tungsten (W) has been chosen as the armor material for the divertor in the International Thermonuclear Experimental Reactor (ITER), and it is a potential candidate for the first wall in future demonstration fusion power reactors (DEMO) considering all the factors of the highest melting point (3422 °C) in metals, sputtering, thermal conductivity, fuel retention and economic reasons [1–3]. During the operation, the armor will experience high heat load with 10 MW/m² heat flux or even higher at a transient state and ELM mode as well as neutron irradiation and helium bombardment. Current operation temperature for W armors is estimated between 200 °C and 1000 °C [4], and will change a little owing to divertor design. Generally, the upper and lower boundary of the operation temperature is determined by the recrystallization temperature and the ductile-brittle transition temperature, respectively. Researchers' payed special attentions on the materials behavior at such high temperatures, because neutron irradiation

and helium trash implantation may result in degradation of W, such as swelling and embrittlement. The temperature dependence of neutron irradiation hardening in W has been reported by Hasegawa et al., correlating irradiation hardening with the microstructure evolution by means of statistical analysis via Orowan type equations [5–8]. More detailed microstructure evolution was investigated by self-ion irradiation experiments with “in-situ” or “ex-situ” methods [9,10]. For example, in shallow (<300 nm) damaged area of ion-irradiated W, the temperature dependent behavior, including the natures of dislocation loops [10,11], a spatial ordering of loop rafts [12], on-set temperature (around 800 °C) of visible voids/cavities formation, and fully disappearance of dislocation loops at 1400 °C during annealing [9] were made clear. Helium implantation experiments have been carried out as well. Thermal desorption spectroscopy (TDS) revealed that the helium desorption spectra showed two peaks at around 600 °C and 2000 °C [13], which were related with the binding state and strength between helium and sinks in W. As W has a very high displacement threshold energy, about 90 eV in average estimated by the simulation study [14] and 52 eV by the experiment study [15], the helium implantation with energy below 1 MeV cannot impose high displacement damage. Therefore, for the investigation of the helium-defects interaction behavior, the materials were often pre-

* Corresponding author.

E-mail addresses: zx-zhang@iae.kyoto-u.ac.jp (Z.X. Zhang), k-yabuuchi@iae.kyoto-u.ac.jp (K. Yabuuchi), kimura@iae.kyoto-u.ac.jp (A. Kimura).

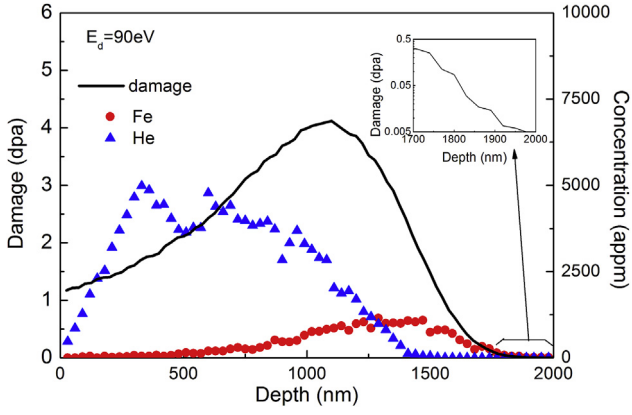


Fig. 1. The profile of damage level, concentration of implanted He and Fe atoms in W calculated by SRIM-2013, with “Ion Distribution and Quick Calculation of Damage” TRIM calculation type. The threshold energy was set as 90 eV and lattice binding energy 0 eV. The implantation energy of Fe^{3+} is 6.4 MeV, and He^+ is 1 MeV, 737 keV, 467 keV and 201 keV. The inset shows the damage between 1700 nm and 2000 nm with logarithmic Y-axis.

damaged by heavy ions irradiation [16] or simultaneously irradiated with a dual-ions, the heavy ions and helium ions [17]. However, such kind of researches particularly on the microstructure evolution are quite limited.

In the case of ion-irradiation experiment, characteristic phenomena lay on the heterogeneous microstructures distributed in the depth direction, which was generally attributed to either the damage profile or implanted atoms concentration profile. A nominal displacement value at a certain depth was usually selected to describe the damage level, and statistical analysis was done at this depth [17,18]. However, recent studies demonstrated that the layered microstructure can be formed under the effect of both the free surface and diffusion to the unirradiated deeper area in the

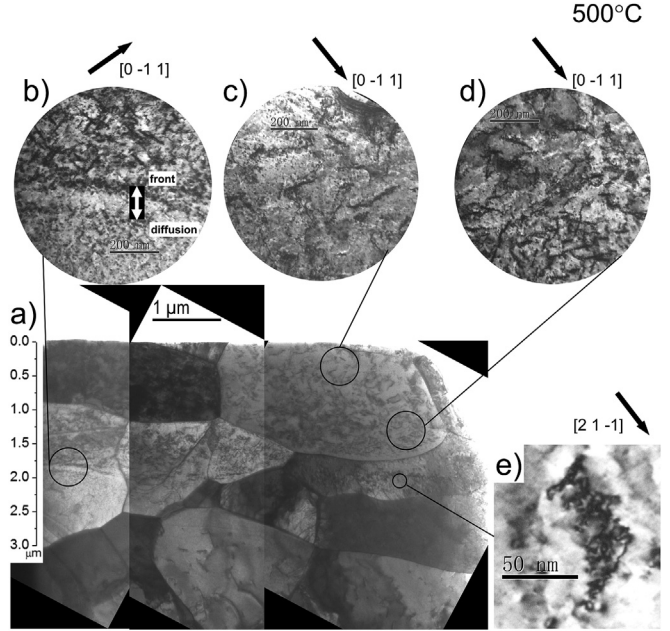


Fig. 3. The microstructure evolution in W irradiated at 500 °C. (b)–(e) Enlarged figures showed the typical morphology of dislocations at different depth under two beam condition. (b) A low dislocation density zone between the front zone and diffusion zone appeared at ~1800 nm. (e) parallel arranged loop rafts in the diffusion zone.

bulk materials [19,20]. Hence, in order to characterize the microstructures induced by ion-irradiation, investigations of a whole view of the distribution of damage structures will be necessary.

The objective of this study is to investigate the whole view of the distribution of damage structures in pure W irradiated with 6.4 MeV Fe^{3+} and energy degraded He^+ with focusing on the irradiation temperature dependence of the distribution

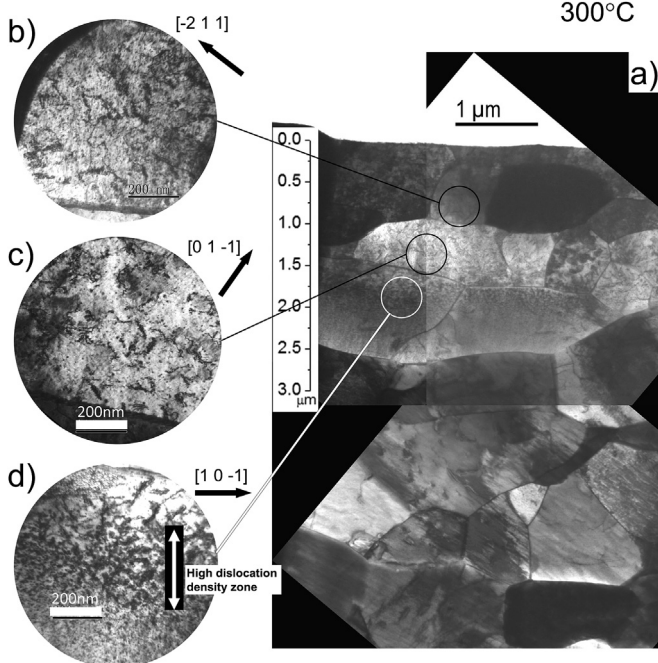


Fig. 2. The microstructure evolution in W irradiated at 300 °C. (b)–(d) Enlarged figures showed the typical morphology of dislocations at different depth under two beam condition. (d) The high dislocation density zone appeared at 1800 nm–2000 nm.

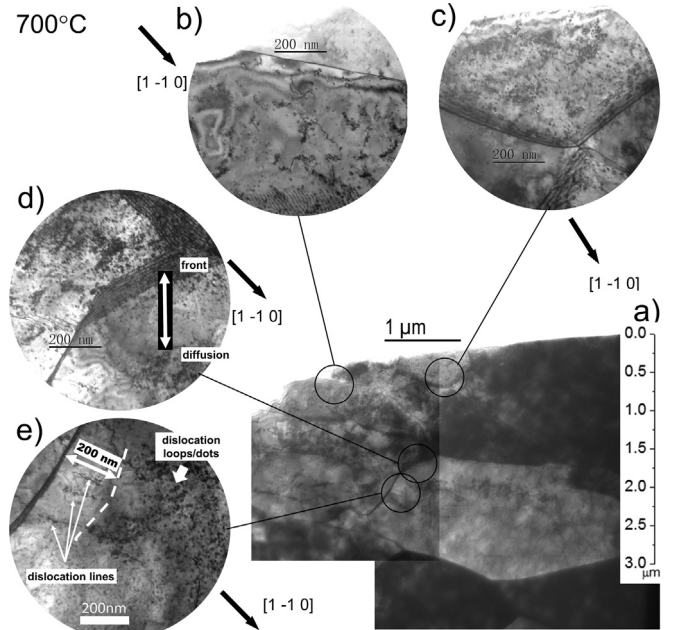


Fig. 4. The microstructure evolution in W irradiated at 700 °C (b)–(e) Enlarged figures showed the typical morphology of dislocations at different depth under two beam condition. (d) The low dislocation density zone between front zone and diffusion zone. (e) The denuded zone near a grain boundary in the diffusion zone.

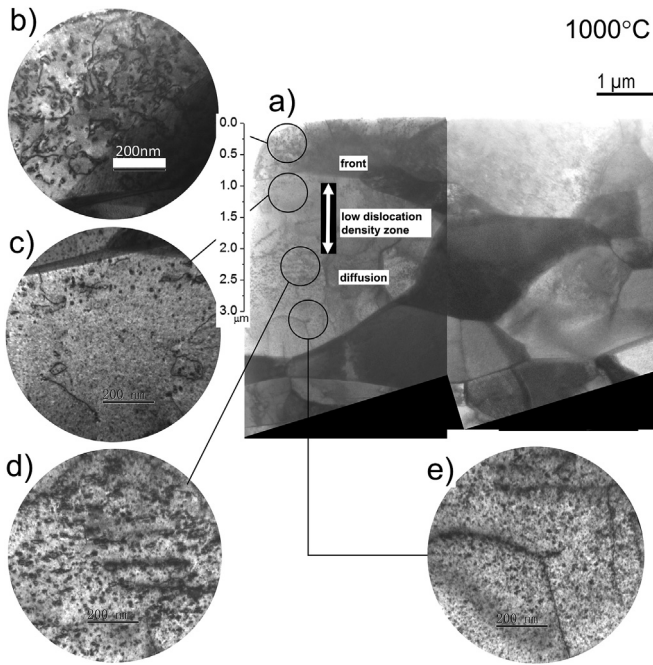


Fig. 5. The microstructure evolution in W irradiated at 1000 °C. (b)–(e) Enlarged figures showed the typical morphology of dislocations at different depth under two beam condition. (d) The loop rafts in the beginning of diffusion zone. (e) Small black dots in the end of diffusion zone.

morphology of damaged structures, such as helium bubbles and dislocation loops. The effects of grain boundaries on the defect distribution is also discussed.

2. Experimental

A rolled W plate with 99.95% purity (Nilaco Co. Ltd) was cut into small specimens (5 mm × 2 mm and thickness 1 mm) for ion-irradiation experiments so that the irradiation surface coincided with the rolling surface. To remove the oxide layer as well as heavily deformed surface layer, the specimens were carefully mechanically

polished by SiC papers of #500, #800, #1200 and #2000, followed by the diamond polishing with the particle sizes of 6 μm, 3 μm, 1 μm, 0.25 μm in sequence. The final electrical polishing was carried out with an electrolyte of 1% NaOH aqueous solution at 20 V for 5 min. The average grain size is about 1.7 μm [21].

Ion-irradiation was performed with a dual ion beam accelerator (DuET) in Kyoto University, which consists of a 1.7 MV tandem accelerator yielding 6.4 MeV Fe³⁺ beam perpendicular to the specimen surface, and a 1.0 MV single-end accelerator yielding He⁺ beam 45° tilted to the specimen [22]. The beams were raster scanned at the frequency 1000 Hz to horizontal direction and 300 Hz to vertical direction. The W specimens were irradiated simultaneously with 6.4 MeV Fe³⁺ and energy-degraded He⁺ from 1 MeV to 737 keV, 467 keV and 201 keV to implant He homogeneously in the W. The irradiation temperatures were 300 °C, 500 °C, 700 °C and 1000 °C. For each temperature, one bulk W specimen was irradiated. The specimens were heated with Joule heating and controlled by the electric current measuring with a pyrometer. The vacuum were at the level of 10⁻⁶ Pa at 300 °C and 10⁻⁵ Pa when above 500 °C. At the end of the irradiation, the electric current was shut down and the specimen was cooled down to room temperature in the vacuum chamber. The depth profile of the ion-irradiation induced displacement damage is calculated by SRIM code using “Quick calculation of Damage” mode with the Kinchin and Pease model following the “energy damage” method introduced by Stoller et al. [23]. The displacement threshold was selected as 90 eV [24]. The results were shown in Fig. 1. The averaged implanted helium within the 1.5 μm depth was 3000 appm. As the He⁺ contributed displacement damage much smaller than Fe³⁺ (dpa_{He}/dpa_{Fe} < 0.1), only Fe³⁺ was considered to the damage calculation and the averaged damage of the irradiated layer was 2 dpa, while the peak value was 4.3 dpa at about 1.1 μm. The damage rate was about 4.4 × 10⁻⁴ dpa/s as an averaged value of the irradiated layer (~2 μm). The total irradiation time was about 70 min with the fluence of Fe and He equals to 5 × 10¹⁹ ion/m² and 2.7 × 10²⁰ ion/m², respectively.

For the cross sectional TEM observation, TEM specimens were prepared by focused ion beam (FIB) system (HITACHI FB2200) with the last beam energy of 40 kV. Flashing electrolytic polishing was carried out at 3 °C to remove the FIB damage in the 0.45% NaOH aqueous solution at a voltage 20 V. The microstructures were

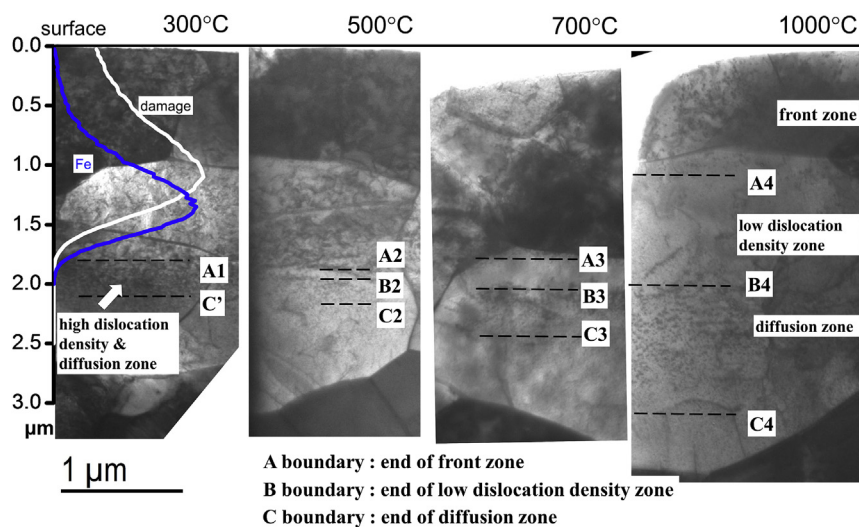


Fig. 6. The whole view of dislocation distribution in the irradiated W at different temperatures. Broken lines indicate the boundary between different zones. Generally, with increasing the irradiation temperature, boundary A will move towards the surface direction, boundary B will remain stable, and boundary C will move to the deeper area. The profiles of damage and Fe concentration calculated by SRIM were shown to compare with the distribution.

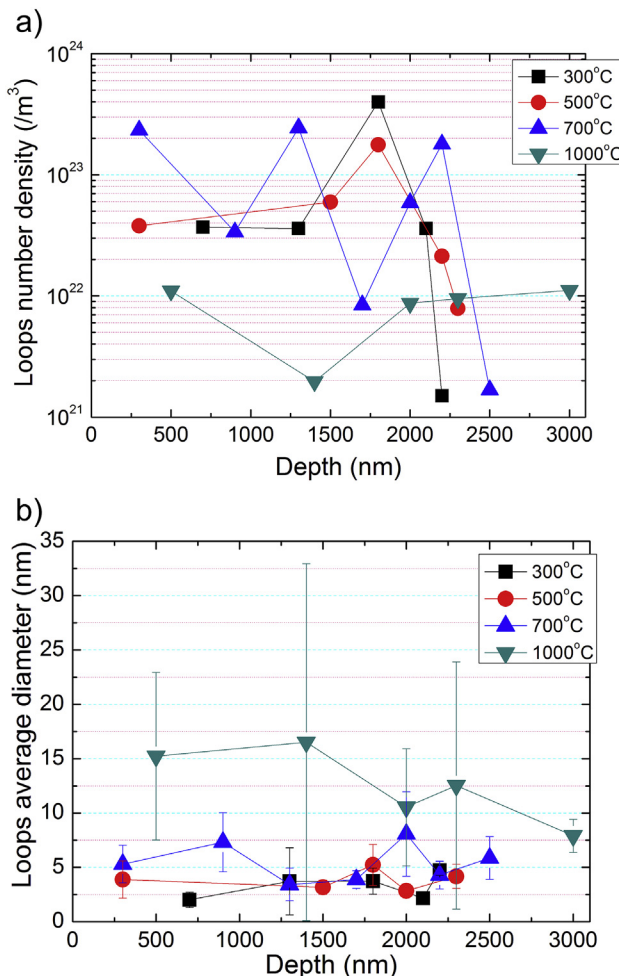


Fig. 7. Statistical analysis of the dislocation loops at each depth, (a) the number density (b) the average diameter.

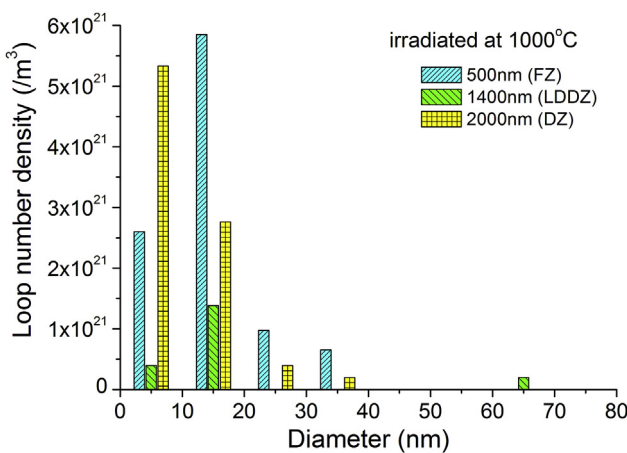


Fig. 8. The histogram of loop size in the different zones irradiated at 1000 °C. FZ: front zone. LDDZ: low dislocation density zone. DZ: diffusion zone.

observed by JEOL JEM-2010 at 200 kV. The distribution of microstructures was investigated for more than two TEM specimens, while the statistical analysis for each depth was taken in a long narrow area in a specimen. The thickness of the TEM specimens was measured by extinction fringes under g3g condition or

convergent beam electron diffraction (CBED) method. The thicknesses of the several TEM specimens were ranging between 30 nm and 80 nm for each. Generally the thickness difference in an observed whole view of the ion-irradiation induced damaged area is estimated to be less than 10 nm based on the extinction fringes analysis.

3. Results

3.1. Whole view of the microstructure evolution in irradiated area

To elaborate the irradiation temperature dependence of microstructure distribution and typical microstructure evolution in ion-irradiated W, the whole views of the TEM specimens irradiated at 300 °C, 500 °C, 700 °C and 1000 °C were observed and shown in Figs. 2, 3 and 5, respectively. Both the irradiated and unirradiated area were shown in each figure. Even though the FIB damages were not completely removed by flashing polish as some small dots could be seen in the unirradiated area, the images were clear enough to recognize the irradiation-induced microstructures in the irradiated area. Typical microstructures in the irradiated area were selected to be shown with a high magnification, which are the bright field images taken at two beam condition. In all the specimens, generally, there is a near surface area where the microstructures were distributed rather homogeneously (with a low dislocation density gradient), which is located from the irradiated surface to a depth where the number density of defects changed dramatically. This area was named as “front zone (FZ)” hereafter. At 300 °C, the dislocation loop-aggregates and dislocation lines could be seen in Fig. 2 (b) and (c) in the FZ. In Fig. 2 (d), a high dislocation density zone (HDDZ) was shown at the depth around 1800 nm to 2000 nm. The dislocation loops tended to form into needle-like aggregates arranged in some directions, which may be correlated with a special crystal orientation. The dislocation density changed dramatically from HDDZ to the deeper bulk area, and completely disappeared within a short distance (<200 nm).

Fig. 3 showed the W irradiated at 500 °C, where the HDDZ was not observed. Instead, the diffusion zone (DZ), which began at depth about 2 μm, became significant. The reason why we call it “diffusion zone” will be discussed in Section 3.2.1. Striking phenomenon appeared in Fig. 3 (b), where the FZ and DZ were separated by a low dislocation density zone (LDDZ), which is only ~100 nm wide. In the LDDZ, dislocations seldom existed at a quite lower density than in the FZ. In the FZ (see Fig. 3 (c) and (d)), loop-

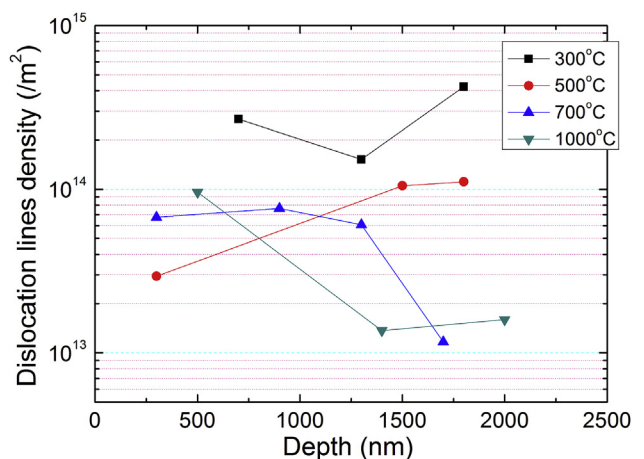


Fig. 9. Depth profile of the density of dislocation lines at different irradiation temperatures.

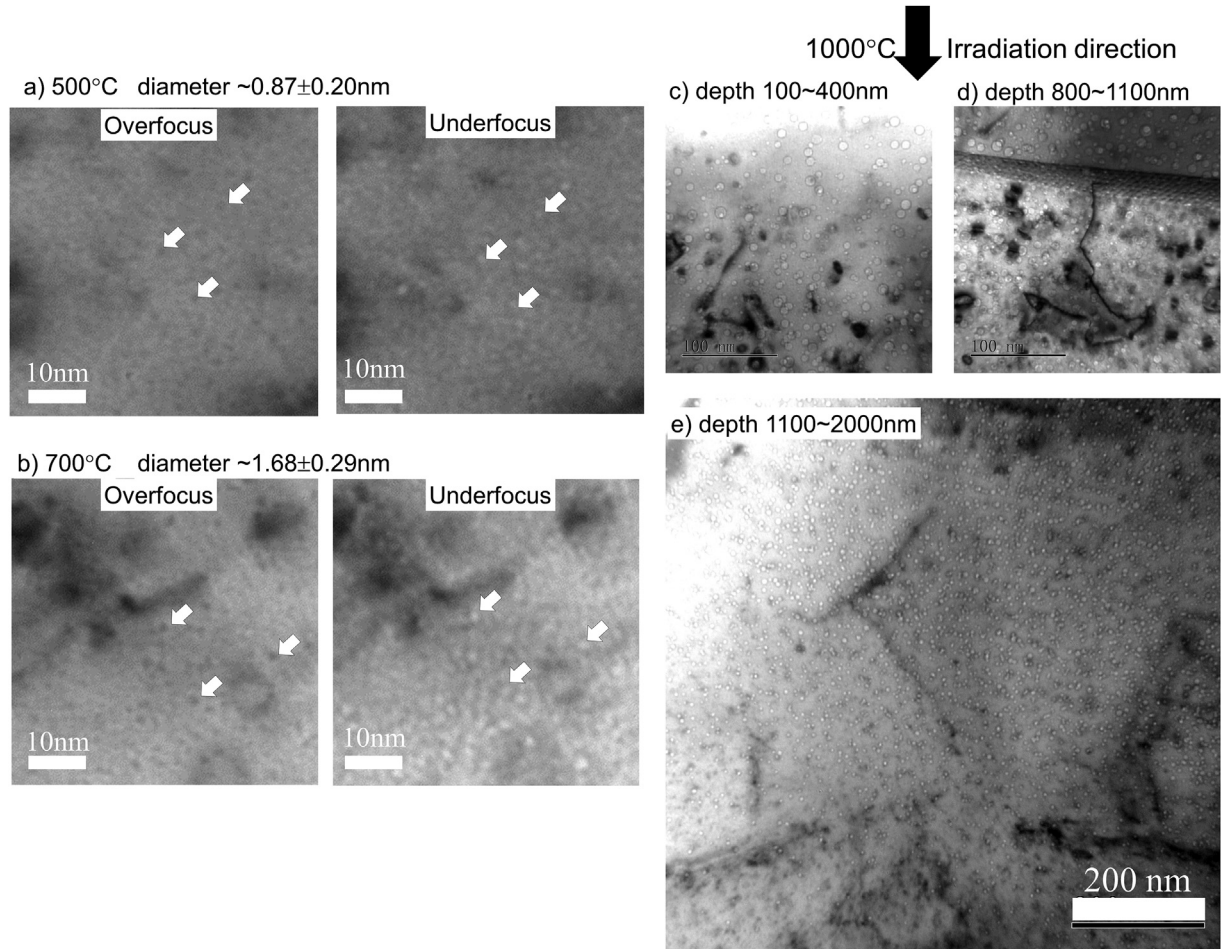


Fig. 10. Bubbles morphology irradiated at (a) 500 °C, (b) 700 °C in the front zone, and (c)–(d) 1000 °C in the front zone, (e) 1000 °C in the low dislocation density zone. Images were observed with the over-focus/under-focus technique.

aggregates are visible. Fig. 3 (e) shows an example of loop-aggregates in the DZ, where the dislocation loops were formed into a one-dimensional loop raft, and then the loop rafts were aligned parallel in a queue.

At 700 °C, loop-aggregates and dislocation lines could still be observed, as shown in Fig. 4 (a) and (b). The distance between the

FZ and DZ increased to ~300 nm, as shown in Fig. 4 (c).

At 1000 °C, no loop-aggregate but isolated dislocation loops were observed in the FZ (see Fig. 5 (b)). The width of LDDZ increased to ~800 nm, inside which a small amount of dislocation loops and lines were observed (see Fig. 5 (c)). The DZ extended significantly into the deeper region. The dislocation loops could form into aggregates at the beginning of DZ (see Fig. 5 (d)), but the isolated dislocation loops gradually reduce their size and finally changes the appearance to small dots in deeper area (see Fig. 5 (e)).

Here it should be mentioned that the naming of each zone, such as FZ, HDDZ, LDDZ and DZ, is based on the TEM observations, comparing the size and number density of dislocation loops among zones. Therefore, there would be a transition zone between those zones, and the distribution might be variable due to crystal orientations.

3.2. Temperature dependent microstructure distribution

3.2.1. Dislocations

The whole distributions at different irradiation temperatures were compared in Fig. 6. The damaged area was divided into a few zones, and the borders are shown with the broken lines, A, B and C. The positions of those border lines are different among the figures, indicating that the damage structure distribution is affected by irradiation temperature. Generally, at 300 °C, the areas were divided into two zones: the FZ and the HDDZ. The DZ at this

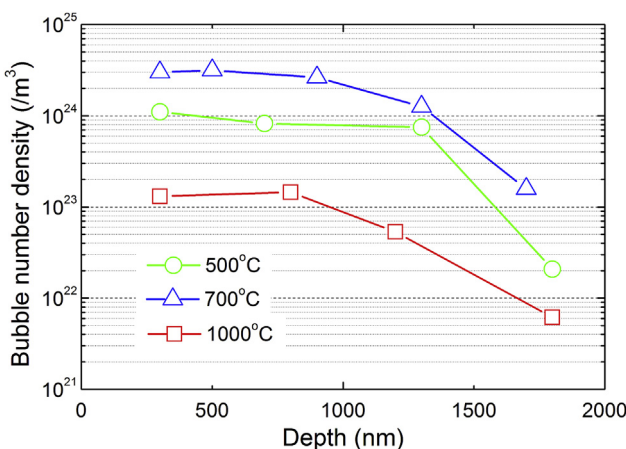


Fig. 11. The depth profile of bubbles number density to depth at 500 °C, 700 °C and 1000 °C.

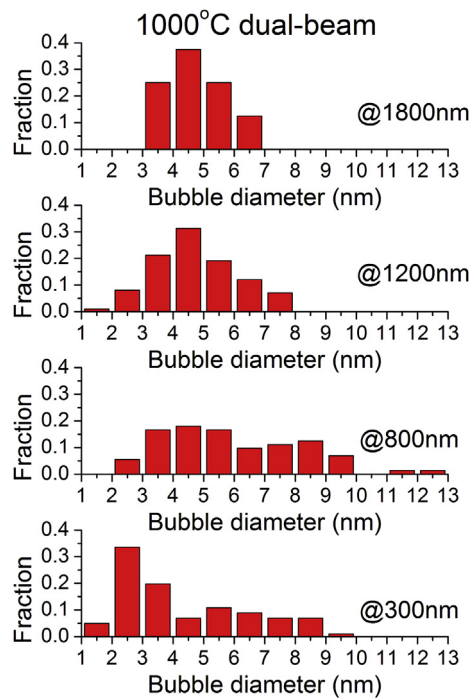


Fig. 12. The distribution of bubble diameter at different depths irradiated at 1000 °C.

temperature is not significant. The HDDZ begins at the depth about 1800 nm, but it disappears at temperature above 500 °C. Similar results were reported in Ref. [19]. The new finding here is the LDDZ appeared at 500 °C and above. The interesting is that with elevating the irradiation temperature, the upper boundary moved towards the surface direction, locating at 1.8 μm at 500 °C, 1.7 μm at 700 °C, and 1 μm at 1000 °C, while the lower boundary of LDDZ stayed at ~2 μm irrespective of irradiation temperature. The location of the zones appears to change a little in different grains, which is considered to be due to the crystal orientation dependence, such as channeling or focusing effect during irradiation [25], but the general distribution of the zones follows the trend described above.

There are several reasons for the naming of DZ: (1) The size and number density of the dislocation loops in DZ gradually decreased with increasing the depth, which can be related with the concentration gradient of defects. (2) With increasing the irradiation temperature, the DZ extended to deeper area, indicating that the diffusion process is involved in the formation of the zone. (3) The interstitial atoms have a higher mobility than vacancies. The migration energy of vacancy in W was calculated to be 1.73 eV [26] or 1.78 eV [27], much higher than self-interstitials in W, which is speculated below 0.08 eV [28,29] or even very close to 0 [30]. (4) No cavity was observed in the DZ.

Dislocation loop rafts appeared at irradiation temperatures from 300 °C to 700 °C. Since the dislocation loops were heavily overlapped, it was difficult to distinguish each dislocation loop and line

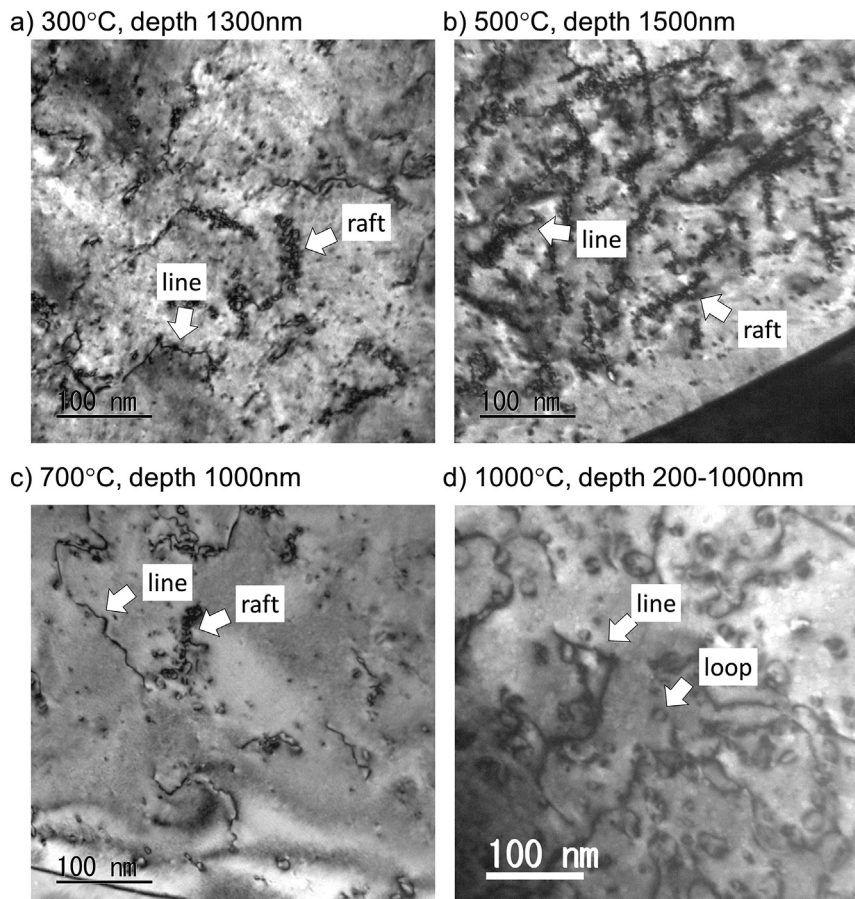


Fig. 13. The typical microstructure in the front zone of dual-ion beam irradiated W at different temperatures. All the images showed dislocation lines and loops. At 300 °C–700 °C, the dislocation loops tended to form into rafts. At 1000 °C, the loops were isolated and no rafts were formed.

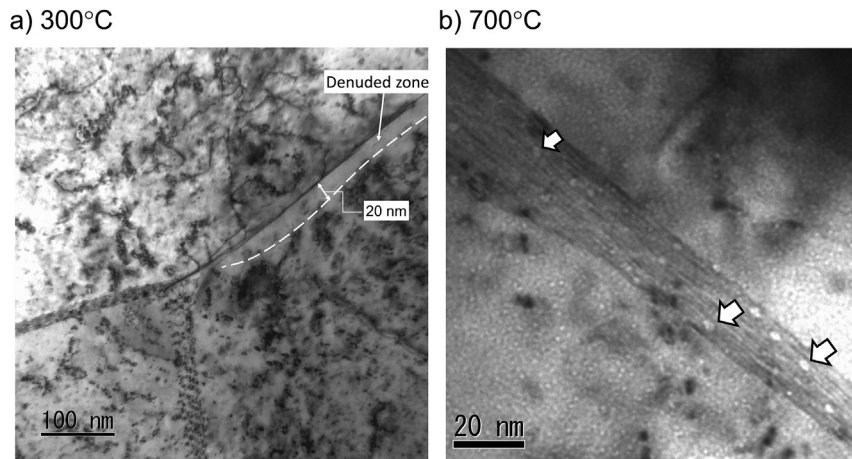


Fig. 14. The influence of grain boundary on (a) dislocations, where a denuded zone appeared with width ~20 nm, (b) helium bubbles, where inside the grain boundaries, the bubbles were with lower number density and larger size than in matrix. Both of the images were in the front zone.

inside. Therefore, the statistical work have to be done in a relatively thin area. Fig. 7 showed the depth profile of the number density and averaged diameter of dislocation loops in the dual-ion beam irradiated W at each temperature. At 300 °C and 500 °C, the number density of dislocation loops appeared to be almost the same at a value about $3 \times 10^{22}/\text{m}^3$. The loop size showed no significant change in the irradiated area. At 1000 °C, there was no raft formation in the FZ. The number density of dislocation loops at this temperature decreased dramatically in comparison to those at the lower temperatures. In the FZ and DZ, it was about $1 \times 10^{22}/\text{m}^3$; while in the LDDZ, it was one order of magnitude lower. On the contrary, the size of dislocation loops increased remarkably in the LDDZ. In Fig. 5 (b) and (c), the existence of irregular shape of dislocation loops with diameter over 50 nm indicates that dislocation loops could merge into a larger loop at 1000 °C. The behavior can be correlated with the in-situ observation in self-ion irradiated tungsten [9]. Fig. 8 showed the histogram of dislocation loop size in FZ (~500 nm), LDDZ (~1400 nm) and DZ (~2000 nm) at 1000 °C. It was clear that the loop diameter is distributed in a wide range. In the FZ, the dislocation loops with diameter from 10 nm to 20 nm occupied the dominant fraction with the highest number density near $6 \times 10^{21}/\text{m}^3$. In the middle zone, even though the dislocation loop density was small, the loop diameter could reach to even 60 nm. In the DZ, dislocation loop density gradually decreased and the loop rafts appeared again.

The density of dislocation lines was measured by line intercept method [31] as follows:

$$\rho = \frac{N}{L_r t} \quad (1)$$

where ρ is the dislocation density, N is the number of line interception, L_r is the total length of the randomly drawn lines, and t is the foil thickness.

Fig. 9 shows the depth profile of dislocation density, in which each line-loop raft structure was also considered as dislocation line, since there is no easy method to distinguish which part belongs to the dislocation line in a heavily overlapped line-loop aggregate. At 300 °C, the dislocation density appeared to increase above 1500 nm in agreement with the HDDZ as shown in Fig. 2 (d). At 500 °C and 1000 °C, the HDDZ was gradually substituted by LDDZ. The dislocation density was therefore decreased dramatically (about one order of magnitude) in comparison to the FZ.

3.2.2. Helium bubbles

The vacancy clusters in dual-beam irradiated W were considered to be helium bubbles, consisting of both helium atoms and vacancies. Visible helium bubbles appeared above 500 °C, as shown in Fig. 10. The bright field images of bubbles were observed by over-focus/under-focus technique under cavity contrast condition (no diffraction pattern excited). At 1000 °C, the apparent changes in the distribution morphology of helium bubbles were observed as shown in Fig. 10 (c) to (e), where the size and number densities of the bubbles were gradually decreased with increasing the depth, and completely disappeared when reached to the DZ. Co-existence of the bubbles, dislocation loops and lines could be seen in Fig. 10 (d). The formation of bubble or void supper lattice structure has been reported for the neutron irradiated [32] or helium implanted W [33], but no void/bubbles supper lattice was observed in the present study.

The averaged bubble diameters were measured to be 0.87 ± 0.20 nm and 1.68 ± 0.29 nm at 500 °C and 700 °C, respectively. There was no remarkable change in the bubble size along with the irradiation depth. Fig. 11 shows the depth profile of the bubble number densities. Generally, the density of bubbles remained stable in the helium implantation area but started to decrease until fully disappeared at the beginning of the DZ. The number density of bubbles at 1000 °C is about one order of magnitude less than those at 500 °C and 700 °C. Fig. 12 shows the histogram of the averaged diameter of bubbles formed at different depths by the irradiation at 1000 °C. In the FZ (300 nm–800 nm), bubbles with the diameter over 7 nm were observed. At the area deeper than 800 nm, the bubble size was deceased, and at 1200 nm, there was no bubble larger than 7 nm.

4. Discussion

4.1. Formation of dislocation lines

Both dislocation lines and loops were observed at all the irradiation temperatures, as shown in Fig. 13. Compared with the un-irradiated W, the dislocation lines density is higher in the irradiated area. The same result was found in recrystallized W [20]. In self-ion irradiated W, dislocation lines and networks appeared at above 950 °C [9]. At this high temperature, the formation of dislocation lines could be explained in terms of both coalescence and growth of dislocation loops. When the dislocation loops grow and touch the grain boundaries or free surfaces, it will be cut into dislocation

lines.

At lower temperatures, dislocation loops preferred to form into aggregates not merge into larger loops. The detail of the formation process of dislocation is not clear yet. One explanation is that some loops, which is formed at the beginning of irradiation with less number of the other damage structures (other loops, cavities or point defects), could grow much faster than the others. Another formation process is based on the one-dimensional loop raft formation. In W, the dislocation loops will self-arrange along a particular crystal orientation, as observed by in-situ TEM studies in self-ion irradiated W [34]. The aligned dislocation loops might be connected [35] to form into an elongated narrow loop [9], then it may convert into dislocation lines.

4.2. Comparison with SRIM code calculation result

Comparison between the microstructure distribution and SRIM code result was already shown in Fig. 6. At 300 °C, the HDDZ located beyond the peaks of both damage and Fe concentration. Therefore, the HDDZ is considered not related to the peak damage level, which is different from traditional considerations that the density of dislocations should be correlated with the damage profile, namely, the dislocation density ought to be highest at the peak position of the damage profile. There is no correlation between the implanted atoms formed the HDDZ. Ciupinski et al. [36] compared the microstructure distribution in W irradiated to different damage levels from 0.01 dpa to 0.89 dpa (peak position), and showed that the HDDZ was formed in the area where the displacement damage level is two orders of magnitude smaller than that of the peak position in 0.89 dpa irradiation. Thus they concluded that the HDDZ is formed at an area with low damage level rather than high damage level. In Fig. 1, the damage level from 1700 nm to 2000 nm was given with logarithm axis. The HDDZ may fit with the damage from 0.005 dpa to 0.05 dpa.

At 500 °C and above, the FZ was suppressed and the DZ was enhanced. SRIM code only works for the case of 0 K, and it could not simulate the thermal effect. Therefore, the prediction of the microstructural distribution by damage level and implanted atom concentration will not be adequate especially for the case of irradiation at elevated temperatures. The factors that influence the microstructure distribution include damage level, implanted atoms concentration, crystal orientations, irradiation temperature, and distance to free surfaces (in the case of irradiation in thin foil). In order to understand the effect of ion-irradiation on the microstructure, TEM observation of the whole distribution morphology of defects is necessary.

4.3. Grain boundary effect

The distribution of defects was also affected by grain boundaries. Because the grain boundaries could act as a sink site for irradiation defects, there will be a dislocation loop denuded zone appearing along the grain boundaries. Fig. 14 (a) shows the microstructure morphology near and inside the grain boundary in FZ, indicating that the denuded zone extended about 20 nm away from the grain boundary. However, in Fig. 4 (d), the denuded zone was as wide as 200 nm in the DZ. The reason is not clear but it may be related with the formation mechanism of the dislocation loops.

Fig. 14 (b) shows that the bubble growth was stimulated in grain boundaries in comparison to those in the matrix. The similar phenomenon was observed in helium implanted W with ultrafine and nano-crystalline grains, where the helium bubbles were mainly assembled on grain boundaries [37]. The number density of the enlarged bubbles in the grain boundary was much smaller than in matrix, which could be owing to bubble growth through the easy

migration of bubbles, or helium-vacancy complexes, along the grain boundary than in the matrix.

In this study, the different effects of grain boundaries were observed between the formations of dislocation loops and bubbles. There was dislocation loop denuded zone nearby grain boundaries but no such a zone for bubbles. Therefore, it is considered that grain boundaries absorb interstitial atoms and its clusters, while the absorption of vacancies and their clusters is limited.

5. Conclusion

The rolled pure W was simultaneously irradiated with 6.4 MeV Fe³⁺ and energy degraded He⁺ from 1 MeV at different temperatures: 300 °C, 500 °C, 700 °C and 1000 °C. The obtained main results are as follows:

- 1) The microstructure distribution is not homogeneous in the damaged area, and remarkably affected by the irradiation temperature.
- 2) At 300 °C, a number of dislocation loops were observed in the front zone (FZ) near the irradiation surface. There is a high dislocation density zone (HDDZ) with high number density of dislocation loops and their aggregates at the end of damaged area.
- 3) At higher temperatures, the HDDZ gradually disappeared and substituted by the low dislocation density zone (LDDZ). The defect diffusion zone (DZ) beyond the damaged area became deeper as irradiation temperature increased.
- 4) Dislocation loops formed into loop raft along particular crystal orientation at 700 °C and below.
- 5) Both dislocation lines and loops were observed in all the irradiated temperatures, while bubbles were observed only at 500 °C and above. The bubble size was stable up to 700 °C, but it increased dramatically at 1000 °C. No bubble was found in the diffusion zone.
- 6) Dislocation loop denuded zone was observed along grain boundaries. The size of denuded zone is different in the front zone and in the diffusion zone. Bubbles were found with larger size in grain boundaries than in the matrix.

Acknowledgement

Mr. Hashitomi and Dr. Kondo are acknowledged for operating the irradiation work in DuET, Kyoto University. China Scholarship Council was thanked for sponsoring the corresponding author.

References

- [1] V. Philippis, J. Nucl. Mater. 415 (2011) S2.
- [2] T. Hirai, F. Escourbiac, S. Carpentier-Chouchana, A. Fedosov, L. Ferrand, T. Jokinen, V. Komarov, A. Kukushkin, M. Merola, R. Mitteau, R.A. Pitts, W. Shu, M. Sugihara, B. Riccardi, S. Suzuki, R. Villari, Fusion Eng. Des. 88 (2013) 1798.
- [3] R.A. Pitts, S. Carpentier, F. Escourbiac, T. Hirai, V. Komarov, S. Ligso, A.S. Kukushkin, A. Loarte, M. Merola, A.S. Naik, R. Mitteau, M. Sugihara, B. Bazylev, P.C. Stangeby, J. Nucl. Mater. 438 (2013) S48.
- [4] H. Bolt, V. Barabash, G. Federici, J. Linke, A. Loarte, J. Roth, K. Sato, J. Nucl. Mater. 307 (2002) 43.
- [5] A. Hasegawa, M. Fukuda, T. Tanno, S. Nogami, Mater. Trans. 54 (2013) 466.
- [6] M. Fukuda, A. Hasegawa, T. Tanno, S. Nogami, H. Kurishita, J. Nucl. Mater. 442 (2013) S273.
- [7] M. Fukuda, T. Tanno, S. Nogami, A. Hasegawa, Mater. Trans. 53 (2012) 2145.
- [8] T. Tanno, M. Fukuda, S. Nogami, A. Hasegawa, Mater. Trans. 52 (2011) 1447.
- [9] F. Ferroni, X.O. Yi, K. Arakawa, S.P. Fitzgerald, P.D. Edmondson, S.G. Roberts, Acta Mater. 90 (2015) 380.
- [10] X. Yi, M.L. Jenkins, M. Briceno, S.G. Roberts, Z. Zhou, M.A. Kirk, Philos. Mag. 93 (2013) 1715.
- [11] X.O. Yi, M.L. Jenkins, K. Hattar, P.D. Edmondson, S.G. Roberts, Acta Mater. 92 (2015) 163.
- [12] S.L. Dudarev, K. Arakawa, X. Yi, Z. Yao, M.L. Jenkins, M.R. Gilbert, P.M. Derlet, J. Nucl. Mater. 455 (2014) 16.

- [13] Gilliam S, Holden J, George S, Parikh N, Hunn J, Snead L, Downing R. Helium Threat Spectrum Implantation in Tungsten. Ion Beam Materials Analysis and modification Group, University of North Carolina at Chapel Hill.
- [14] Q. Xu, T. Yoshiie, H.C. Huang, *Nucl. Instrum. Methods Phys. Res. Sec. B Beam Interact. Mater. Atoms* 206 (2003) 123.
- [15] J.A. Dicarlo, J.T. Stanley, *Radiat. Eff.* 10 (1971) 259.
- [16] Z. Chen, W.J. Han, J.G. Yu, K.G. Zhu, *J. Nucl. Mater.* 472 (2016) 110.
- [17] Y. Himeji, K. Yabuuchi, R. Kasada, S. Noh, H. Noto, T. Nagasaka, S. Nogami, A. Kimura, *Mater. Trans.* 54 (2013) 446.
- [18] T. Hwang, M. Fukuda, S. Nogami, A. Hasegawa, H. Usami, K. Yabuuchi, K. Ozawa, H. Tanigawa, Effect of self-ion irradiation on hardening and microstructure of tungsten, *Nucl. Mater. Energy* (2016), <http://dx.doi.org/10.1016/j.nme.2016.06.005>.
- [19] J. Grzonka, L. Ciupinski, J. Smalc-Koziorowska, O.V. Ogorodnikova, M. Mayer, K.J. Kurzydlowski, *Nucl. Instrum. Methods Phys. Res. Sec. B Beam Interact. Mater. Atoms* 340 (2014) 27.
- [20] Z.X. Zhang, E. Hasenhuettl, K. Yabuuchi, A. Kimura, Evaluation of helium effect on ion-irradiation hardening in pure tungsten by nano-indentation method, *Nucl. Mater. Energy* (2016), <http://dx.doi.org/10.1016/j.nme.2016.06.010>.
- [21] Z.X. Zhang, D.S. Chen, W.T. Han, A. Kimura, *Fusion Eng. Des.* 98–99 (2015) 2103.
- [22] A. Kohyama, Y. Katoh, M. Ando, K. Jimbo, *Fusion Eng. Des.* 51–52 (2000) 789.
- [23] R.E. Stoller, M.B. Toloczko, G.S. Was, A.G. Certain, S. Dwaraknath, F.A. Garner, *Nucl. Instrum. Methods Phys. Res. Sec. B Beam Interact. Mater. Atoms* 310 (2013) 75.
- [24] ASTM, Standard Practice for Neutron Radiation Damage Simulation by Charged-Particle Irradiation, E521–96, 2009.
- [25] G.S. Was, Fundamentals of Radiation Materials Science: Metals and Alloys, Springer Science & Business Media, 2007.
- [26] R.L. Danilowicz, Point Defect Calculations in Tungsten, DTIC Document, 1968.
- [27] S.I. Dudarev, *Annu. Rev. Mater. Res.* 43 (2013) 35.
- [28] J. Amano, D.N. Seidman, *J. Appl. Phys.* 56 (1984) 983.
- [29] F. Dausinger, H. Schultz, *Phys. Rev. Lett.* 35 (1975) 1773.
- [30] H. Tanimoto, H. Mizubayashi, H. Nishimura, S. Okuda, *J. Physique IV* 6 (1996) 285.
- [31] D.M. Norfleet, D.M. Dimiduk, S.J. Polasik, M.D. Uchic, M.J. Mills, *Acta Mater.* 56 (2008) 2988.
- [32] V.K. Sikka, J. Motteff, *J. Appl. Phys.* 43 (1972) 4942.
- [33] P.B. Johnson, D.J. Mazey, *J. Nucl. Mater.* 218 (1995) 273.
- [34] X.O. Yi, M.L. Jenkins, M.A. Kirk, Z.F. Zhou, S.G. Roberts, *Acta Mater.* 112 (2016) 105.
- [35] K. Arakawa, T. Amino, H. Mori, *Acta Mater.* 59 (2011) 141.
- [36] L. Ciupinski, O.V. Ogorodnikova, T. Plocinski, M. Andrzejczuk, M. Rasinski, M. Mayer, K.J. Kurzydlowski, *Nucl. Instrum. Methods Phys. Res. Sec. B Beam Interact. Mater. Atoms* 317 (2013) 159.
- [37] O. El-Atwani, A. Suslova, T.J. Novakowski, K. Hattar, M. Efe, S.S. Harilal, A. Hassanein, *Mater. Charact.* 99 (2015) 68.